

## Follow-up Studies of Five Cataclysmic Variable Candidates Discovered by LAMOST

JOHN R. THORSTENSEN<sup>1</sup>

<sup>1</sup>*Department of Physics and Astronomy, 6127 Wilder Laboratory, Dartmouth College, Hanover, NH 03755-3528*

### ABSTRACT

We report follow-up observations of five cataclysmic variable candidates from LAMOST published by Hou et al. (2020). LAMOST J024048.51+195226.9 is the most unusual of the five; an early-M type secondary star contributes strongly to its spectrum, and its spectral and photometric behavior are strikingly reminiscent of the hitherto-unique propeller system AE Aqr. We confirm that a 7.34-hr period discovered in the Catalina survey data (Drake et al. 2014) is orbital. Another object, LAMOST J204305.95+341340.6 appears to be a near twin of the novalike variable V795 Her, with an orbital period in the so-called 2-3 hour “gap”. LAMOST J035913.61+405035.0 is evidently an eclipsing, weakly-outbursting dwarf nova with a 5.48-hr period. Our spectrum of LAMOST J090150.09+375444.3 is dominated by a late-type secondary and shows weak, narrow Balmer emission moving in phase with the absorption lines, but at lower amplitude; we do not see the He II  $\lambda 4686$  emission evident in the published discovery spectrum. We again confirm that a period from the Catalina data, in this case 6.80 hr, is orbital. LAMOST J033940.98+414805.7 yields a radial-velocity period of 3.54 hr, and its spectrum appears to be typical of novalike variables in this period range. The spectroscopically-selected sample from LAMOST evidently includes some interesting cataclysmic variables that have been unrecognized until now, apparently because of the relatively modest range of their photometric variations.

*Keywords:* keywords: stars

### 1. INTRODUCTION

Cataclysmic variable stars (CVs) are binary systems in which a white dwarf accretes matter from a companion via Roche lobe overflow. The companion usually resembles a main-sequence star, but often shows significant differences, from some combination of nuclear evolution and the effects of having transferred significant mass (Knigge 2006; Knigge et al. 2011). CV orbital periods  $P_{\text{orb}}$  range from  $\sim 5$  min for the most extreme double-degenerate systems, up to several days for systems that have evolved significantly, but more typically range from  $\sim 80$  min up to  $\sim 10$  hr for hydrogen-burning secondaries. Warner (1995) gives an overview of these objects; Goliaš & Nelson (2015) and Kalomeni et al. (2016) describe models of CV evolution.

CVs fall into several subclasses, some of them overlapping. Many are dwarf novae, which from time to time undergo brightenings (called *outbursts*). The outbursts are thought to be caused by an instability triggered when the accretion disk reaches a critical density. In another class, called novalike variables, the mass-transfer rate from the secondary star is large enough to maintain the disk in a bright state; some novalikes fade into low states, apparently when mass transfer slows or stops. In some CVs the white dwarf is highly magnetized, which affects the accretion flow. In AM Herculis stars, also called *polars*, no disk forms, the white dwarf co-rotates with the orbit, and the magnetic field channels the accretion flow onto the magnetic poles of the white dwarf. If the white dwarf field is somewhat smaller, the accretion disk is not entirely disrupted, and the white dwarf does not co-rotate with the orbit. In such systems, called DQ Herculis stars or *intermediate polars*, the brightness is often modulated at the white dwarf rotation period or an orbital sideband. Some intermediate polars show dwarf nova outbursts (for example, EX Hya; Beuermann et al. 2003), but more typically they are novalike variables.

CVs are discovered through several different channels, all of which are biased in one way or another. Most cataloged CVs are dwarf novae. Dwarf novae are usually discovered because of their outbursts, which trigger variability surveys such as the Catalina surveys (Drake et al. 2009; Breedt et al. 2014), ASAS-SN (Shappee et al. 2014), MASTER (Lipunov et al. 2010), and ATLAS (Tonry et al. 2018). Many CVs have been discovered as X-ray sources, especially

the magnetic subtypes (see [Schwope 2018](#) and references therein). Most CVs have unusual colors, and were discovered in spectroscopic or variability follow-ups of color-selected objects ([Green et al. 1982](#); [Szkody et al. 2011](#)). CVs can have strong emission lines (though not all do), which stand out in spectroscopic surveys ([Aungwerojwit et al. 2006](#); [Witham et al. 2008](#)). Even with all these means of discovery, the sample of known CVs is apparently not representative; as one example, [Pala et al. \(2020\)](#) examine a volume-limited sample of CVs within 150 pc of earth, as determined by Gaia DR2 parallaxes, and find that over 30 per cent are magnetic CVs, far in excess of their numbers in other catalogs. It is therefore always a welcome development when new CV samples become available using novel selection methods.

Recently, [Hou et al. \(2020\)](#) presented just such a sample. They examined spectra from the Large Sky Area Multi-Object Fiber Spectroscopic Telescope (LAMOST) using machine-learning techniques, and selected 245 CV candidates from among the millions spectra produced by the survey. While most of their sample had already been identified as CVs, 58 of their candidate CVs apparently had not been previously been recognized as such.

In this paper we present initial optical follow-up studies of five of these new objects. We set out to verify that they are CVs, assess their subtypes, determine reliable orbital periods  $P_{\text{orb}}$  when possible.

Table 1 gives basic information on the stars we observed; for brevity, we will sometimes abbreviate their names. The distances quoted are simple inverses of the Gaia parallaxes, which have relative errors small enough to be accurate enough for our purposes. We used the Gaia distances together with the [Green et al. \(2019\)](#) 3-D reddening maps<sup>1</sup> to estimate the tabulated reddenings  $E(g - r)$ . The approximate absolute  $G$  magnitudes are calculated using the central value of the distance, and assuming that (a) reddening in  $G$  is comparable to reddening in  $V$ , and (b)  $E(B - V) \sim E(g - r)$  (see the discussion at <http://argonaut.skymaps.info/usage#versions>). Note that  $M_G$  should be comparable to  $M_V$ , since  $G$  and  $V$  magnitudes differ by only a few tenths for normal blue ( $B - V < 0.5$ ) stars (see Fig. 15 of [Carrasco et al. 2016](#)).

The plan of the paper is as follows. Section 2 describes our observation, reduction and analysis procedures. The results for the individual stars are given in Section 3, in order of right ascension. Table 2 gives the measured radial velocities, and Table 3 gives parameters of sinusoidal fits to the velocities. We summarize our results in Section 4.

## 2. TECHNIQUES

All the data presented here were taken in 2019 December and 2020 January, at MDM Observatory on Kitt Peak, Arizona.

All our spectra are from the 2.4m Hiltner reflector with the Ohio State Multi-Object Spectrometer (OSMOS; [Martini et al. 2011](#)) used in single-slit mode. We used the “blue” disperser, with the 1.1-arcsecond “inner” slit, yielding  $\sim 3.1$  Å resolution (FWHM) from 3980 to 6860 Å, and a dispersion of 0.7 Å per 15  $\mu\text{m}$  pixel. The CCD detector we used has four amplifiers, so we used a python script to compute and subtract bias levels from each quadrant. For spectroscopic flat fields we used spectra of an incandescent bulb. As a check, we also created flat field images from spectra of the sky taken soon after sunset. To eliminate the strong solar spectrum from these, we divided the data in each column (i.e., at each wavelength) by a polynomial fitted to that column. The sky-derived flats were nearly identical to those from the bulb, but had slightly poorer signal-to-noise.

To extract one-dimensional spectra from the images, we used a new python implementation of the variance-weighted algorithm described by [Horne \(1986\)](#)<sup>2</sup>. To calibrate the wavelength scale, we took exposures of Hg, Ne, and Xe comparison lamps in the zenith during the day, and then bracketed our science exposures with short Hg-Ne exposures to track the drift in the zero point and the dispersion (which did change significantly) with telescope position and ambient temperature. The resulting calibration was typically accurate to  $\sim 10$  km s<sup>-1</sup>, judging from night-sky features ([Osterbrock et al. 1996](#)). When the sky was clear and the seeing acceptable, we observed flux standard stars from which we derived a flux calibration.

We measured emission-line radial velocities by convolving the line profiles with antisymmetric functions and looking for the zero of the convolution ([Schneider & Young 1980](#); [Shafter 1983](#)). With this method one can vary the width and functional form of the antisymmetric function to emphasize or exclude different parts of the line profile. Each pixel in the spectrum has an uncertainty estimate based on the gain, background, read noise, and flux; we propagated those through the measurement process to estimate the uncertainty  $\sigma_i$  in each velocity  $v(t_i)$ , or rather a lower limit, since the estimate does not include systematic errors.

<sup>1</sup> See <http://argonaut.skymaps.info/>

<sup>2</sup> The program is available at <https://github.com/jrthorstensen/opextract>.

The spectra of several of these the objects showed contributions from late-type stars. To measure the velocities of the late-type component, we cross-correlated the spectrum against late-type template spectra, using the IRAF task `fxcor`, after masking out regions around emission lines. For the templates, we used averaged spectra of late-type stars with accurately-known velocities; the individual stars had been shifted into the rest frame before averaging. The template spectra were originally taken with the *modspec* spectrograph on the 2.4 m telescope.

To search for periods, we constructed a dense grid of trial frequencies covering from near zero to 20 cycles per day, fit least-squares sinusoids at each frequency, and plotted  $1/\chi^2$  versus frequency, where

$$\chi^2 = \sum_i \frac{(v(t_i) - c_i)^2}{\sigma_i^2}, \quad (1)$$

$v(t_i)$  is the velocity measured at time  $t_i$ , and  $c_i$  is the expected value at  $t_i$  computed using the best-fit sinusoid. Even in well-sampled data these “residual-grams” invariably show possible fits at several frequencies separated by 1 cycle  $\text{d}^{-1}$ , because velocities from a single site cannot be taken during daytime; this causes ambiguity, or aliasing, in the daily cycle count. To mitigate this, we included observations with as wide a spread of hour angles – essentially times *modulo* one day – as we could manage. At large hour angles, differential atmospheric refraction (Filippenko 1982) can be severe, so when necessary we rotated the instrument to orient the slit near the parallactic angle.

We fit the radial velocity time series with least-squares sinusoidal functions of the form

$$v(t) = \gamma + K \sin \left[ \frac{2\pi(t - T_0)}{P} \right], \quad (2)$$

and estimated parameter uncertainties from the goodness of fit. Table 3 shows the parameters for all the targets.

To acquire a spectroscopic target with OSMOS, one first obtains a direct image of the field by removing the disperser and slit from the beam (configuring the instrument as a reducing camera) and taking a brief (typically 20 s) exposure. Using this image, one fine-tunes the telescope position so that after the slit is returned to the beam, the target will fall in the slit. To enhance the scientific value of these acquisition images, we took them with a Sloan *g* filter. The images covered  $4.6 \times 18.4$  arcmin, and therefore included many field stars as well as the target. To efficiently calibrate the targets’ *g* magnitudes, we developed a procedure that (1) automatically generates an astrometric solution by matching the stars in the image to their entries in the Pan-STARRS 1 catalog, (2) performs aperture photometry on the field star images, (3) finds the mean offset between the aperture-photometry magnitudes and Pan-STARRS  $g_{\text{PSF}}$ , and (4) applies this offset to the target’s aperture magnitude. The scatter in the magnitude offset was small, typically only a few hundredths of a magnitude for well-exposed stars. The procedure also yields a measure of the image quality, (which for some of our observations was remarkably poor); the size of the magnitude offset is also sensitive to seeing and transparency variations.

For some of our targets, we also obtained differential time-series photometry using the 1.3-meter McGraw-Hill telescope. In 2019 December we used a SITe CCD detector cropped to a  $256 \times 256$  sub-array of  $0''.508$  pixels, and in 2020 January we used an Andor IKON camera with a frame-transfer CCD. All the images were essentially ‘white light’, being filtered only by a Schott GG420 glass filter, which passes  $\lambda > 4200 \text{ \AA}$  and therefore helps suppress scattered moonlight. In each image we measured instrumental magnitudes for the program star, a comparison star, and several check stars using the aperture photometry code in the IRAF implementation of DAOPHOT. While the raw data are uncalibrated and differential, we adjust them here to approximate standard magnitudes using catalog magnitudes of the comparison stars. Because the original images were basically unfiltered, we estimate the zero point to be uncertain by several tenths of a magnitude.

### 3. THE INDIVIDUAL STARS

#### 3.1. LAMOST J024048.51+195226.9

The LAMOST spectrum (Hou et al. 2020) shows strong Balmer lines, but rather weak features of He I and no evident He II lines; the continuum shows wide absorption bands indicating that an M star contributes a significant fraction of the light. The Catalina Real Time Survey light curve (Drake et al. 2009), shown in Fig. 1, shows the source most often just brighter than 17th magnitude, but often brighter than 16.5, and never fainter than about 17.2. There is no evident pattern in the long-term variability, and in particular distinct outbursts are not present. However, Drake et al. (2014) searched the Catalina data for periodic variations and discovered a periodicity at 0.3056840 d, or 7.33555 hr; the lower panel of Fig. 1 shows the same data, folded on this period.

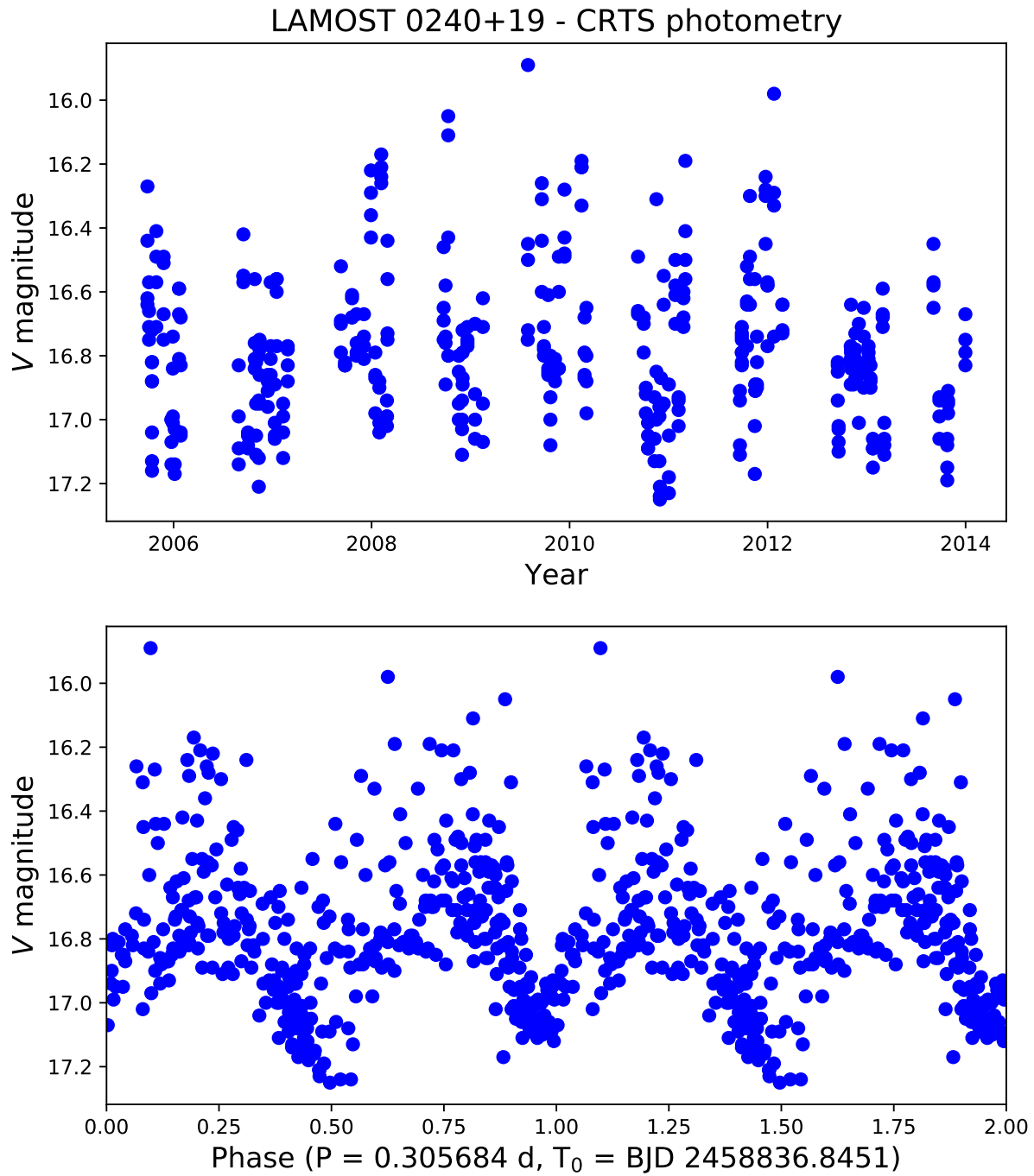


**Figure 1.** Archival photometry of LAM 0240+19 from the CRTS DR2. The top panel shows the data as a function of time, and the bottom panel shows the data folded on the period found by [Drake et al. \(2014\)](#). Phase zero corresponds to inferior conjunction of the secondary star, as deduced from the absorption-line radial velocities.

**Table 1.** List of Objects

Name	$\alpha_{\text{ICRS}}$ [h:m:s]	$\delta_{\text{ICRS}}$ [d:m:s]	$G$	$1/\pi_{\text{DR2}}$ [pc]	$E(g-r)$	$M_G$
LAMOST J024048.51+195226.9	02:40:48.531	+19:52:26.96	16.8	$627 \pm 36$	0.02	7.8
LAMOST J033940.98+414805.7	03:39:40.991	+41:48:05.69	15.2	$914 \pm 38$	0.17	4.9
LAMOST J035913.61+405035.0	03:59:13.625	+40:50:35.08	17.4	$874 \pm 94$	0.34	6.7
LAMOST J090150.09+375444.3	09:01:50.119	+37:54:44.22	16.9	$525 \pm 28$	0.01	8.3
LAMOST J204305.95+341340.6	20:43:05.955	+34:13:40.73	15.3	$992 \pm 27$	0.35	4.3

NOTE—The celestial coordinates, mean  $G$  magnitudes, and distances are from the GAIA Data Release 2 (DR2; Gaia Collaboration et al. 2016, 2018). Positions are referred to the ICRS (essentially the reference frame for J2000), and the catalog epoch (for proper motion corrections) is 2015. The distances and their error bars are the inverse of the DR2 parallax  $\pi_{\text{DR2}}$ , and do not include any corrections for possible systematic errors. See text for discussion of the last columns ( $E(g-r)$  and  $M_G$ ).

**Table 2.** Radial Velocities

Target	Time	$v_{\text{abs}}$ (km s <sup>-1</sup> )	$\sigma(v_{\text{abs}})$ (km s <sup>-1</sup> )	$v_{\text{emn}}$ (km s <sup>-1</sup> )	$\sigma(v_{\text{emn}})$ (km s <sup>-1</sup> )
LAMOST J024048.51+195226.9	58829.8120	-44	25	...	...
LAMOST J024048.51+195226.9	58829.8194	41	33	...	...
LAMOST J024048.51+195226.9	58829.8286	16	39	...	...
LAMOST J024048.51+195226.9	58829.8360	212	47	...	...
LAMOST J024048.51+195226.9	58830.8746	111	35	...	...
LAMOST J024048.51+195226.9	58830.8834	38	20	...	...

NOTE—Radial velocities used in this study. The full table is published as a machine-readable table; the first few lines are shown here to indicate its form and content.

We observed this star most extensively in 2019 December. Our mean spectrum (Fig. 2, top panel) resembles the LAMOST spectrum. Before averaging, the individual spectra were shifted to the rest frame of the late-type star using the orbital ephemeris (see below). To characterize the late-type component, we subtracted spectra of M-dwarfs classified by Boeshaar (1976), which had been shifted to their own rest frames using velocities from Marcy et al. (1987), and varied the spectral type and flux of the subtracted spectrum to obtain the best cancellation of the late-type features. From this we estimate the secondary spectral type to be  $M1.5 \pm 1$  subclass.

We searched for  $P_{\text{orb}}$  using the the H $\alpha$  emission line velocities, but these showed significant scatter and did not yield a unique period. In contrast, the cross-correlation velocities from the absorption lines varied smoothly on a period of 7.34(2) hr. This was accurate enough to connect the cycle count to spectra obtained in 2020 January; the combined data give 7.3371(8) hr, consistent with the photometric period from Drake et al. (2014) within the mutual uncertainty. The Drake et al. (2014) period is more precise than ours due to the long time base, so we adopt this as the orbital period. The lower panel of Fig. 2 shows the absorption velocities folded on  $P_{\text{orb}}$ .

The absorption-line velocities trace the motion of the secondary star, and therefore establish the binary phase for this non-eclipsing system. The epoch  $T_0$  corresponds to blue-to-red crossing of the secondary star’s velocities, which is

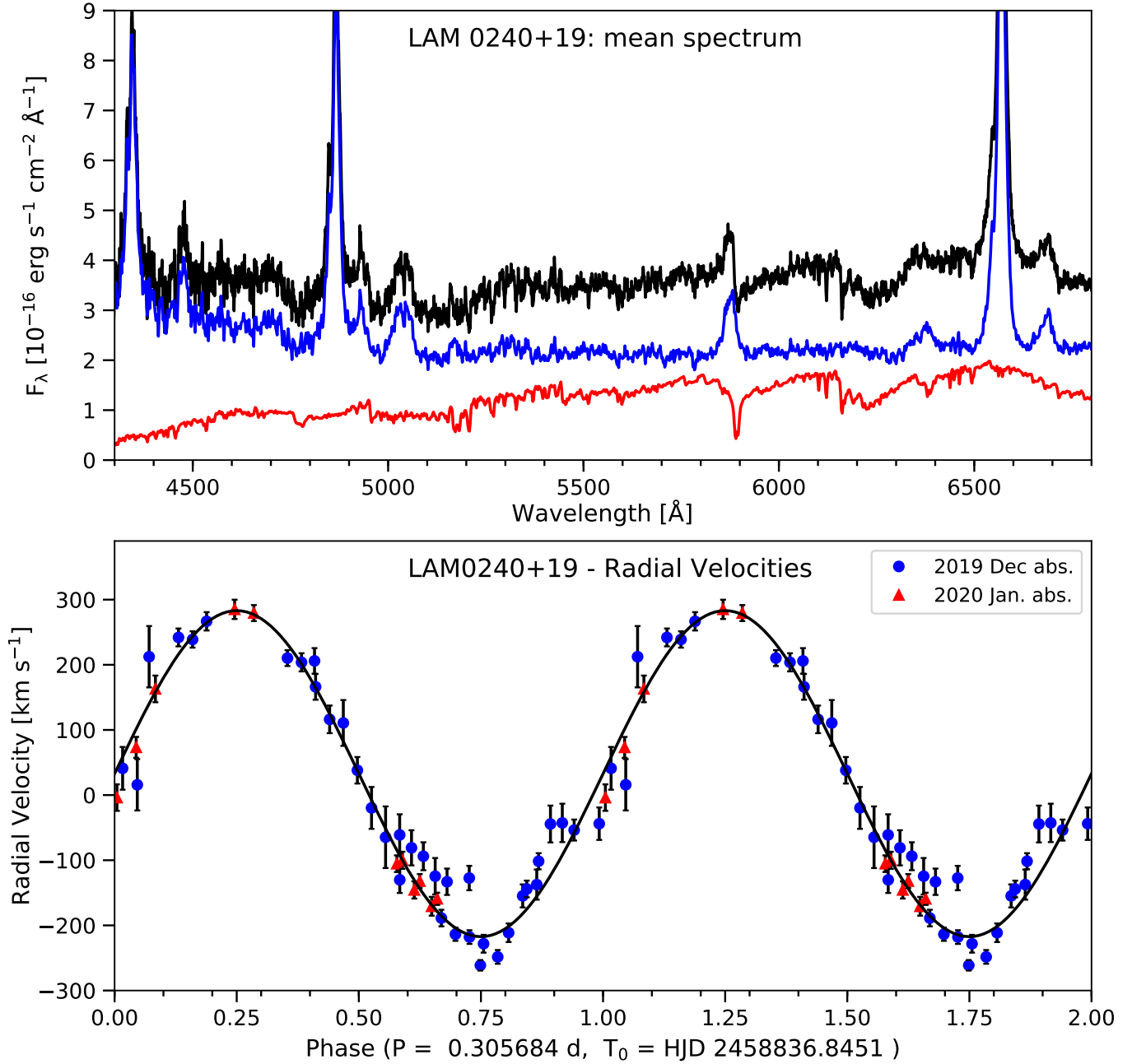


**Figure 2.** Upper panel: The mean spectrum of LAM 0240+19. The top trace (black) is the observed spectrum averaged in the rest frame of the late-type star; the middle trace (blue) shows the same data after subtraction of the spectrum shown in bottom trace (red), which is a scaled spectrum of the M1.5-type dwarf Gliese 15a. Lower panel: Radial velocities of the secondary star, folded on the ephemeris shown. The best-fitting sinusoid is plotted, and the data are repeated through a second cycle for continuity.

**Table 3.** Parameters of Best Fit Sinusoids

Target	Line type	$T_0^a$	$P$ (d)	$K$ (km s <sup>-1</sup> )	$\gamma$ (km s <sup>-1</sup> )	$N$	$\sigma$ (km s <sup>-1</sup> )
LAMOST J024048.51+195226.9	abs.	58836.845(2)	0.305684 <sup>b</sup>	250(8)	33(6)	48	30
LAMOST J033940.98+414805.7	emn.	58832.686(3)	0.14712(18)	182(21)	41(15)	58	50
LAMOST J035913.61+405035.0	abs.	58832.868(5)	0.228344 <sup>c</sup>	215(28)	-53(20)	16	52
LAMOST J035913.61+405035.0	emn.	58833.000(5)	0.228344 <sup>c</sup>	190(33)	-40(21)	35	72
LAMOST J090150.09+375444.3	emn.	58836.1463(17)	0.283387 <sup>b</sup>	101(7)	8(3)	20	12
LAMOST J090150.09+375444.3	abs.	58836.1522(13)	0.283387 <sup>b</sup>	190(8)	6(5)	20	16
LAMOST J204305.95+341340.6	emn. (best)	58832.6260(18)	0.10777(10)	208(19)	-27(15)	28	50
LAMOST J204305.95+341340.6	emn. (alternate)	58832.625(2)	0.12078(14)	210(20)	-13(15)	28	52

NOTE—Fits to radial velocities. The last two columns give the number of points fitted and the root-mean-square residual. Uncertainties are given in parentheses, in units of the last digits quoted.

<sup>a</sup>Barycentric Julian Date, minus 2,400,000., in the UTC time scale.

<sup>b</sup>Period fixed at the value given by Drake et al. (2014).

<sup>c</sup>Period fixed by the provisional eclipse ephemeris (Eqn. 3).

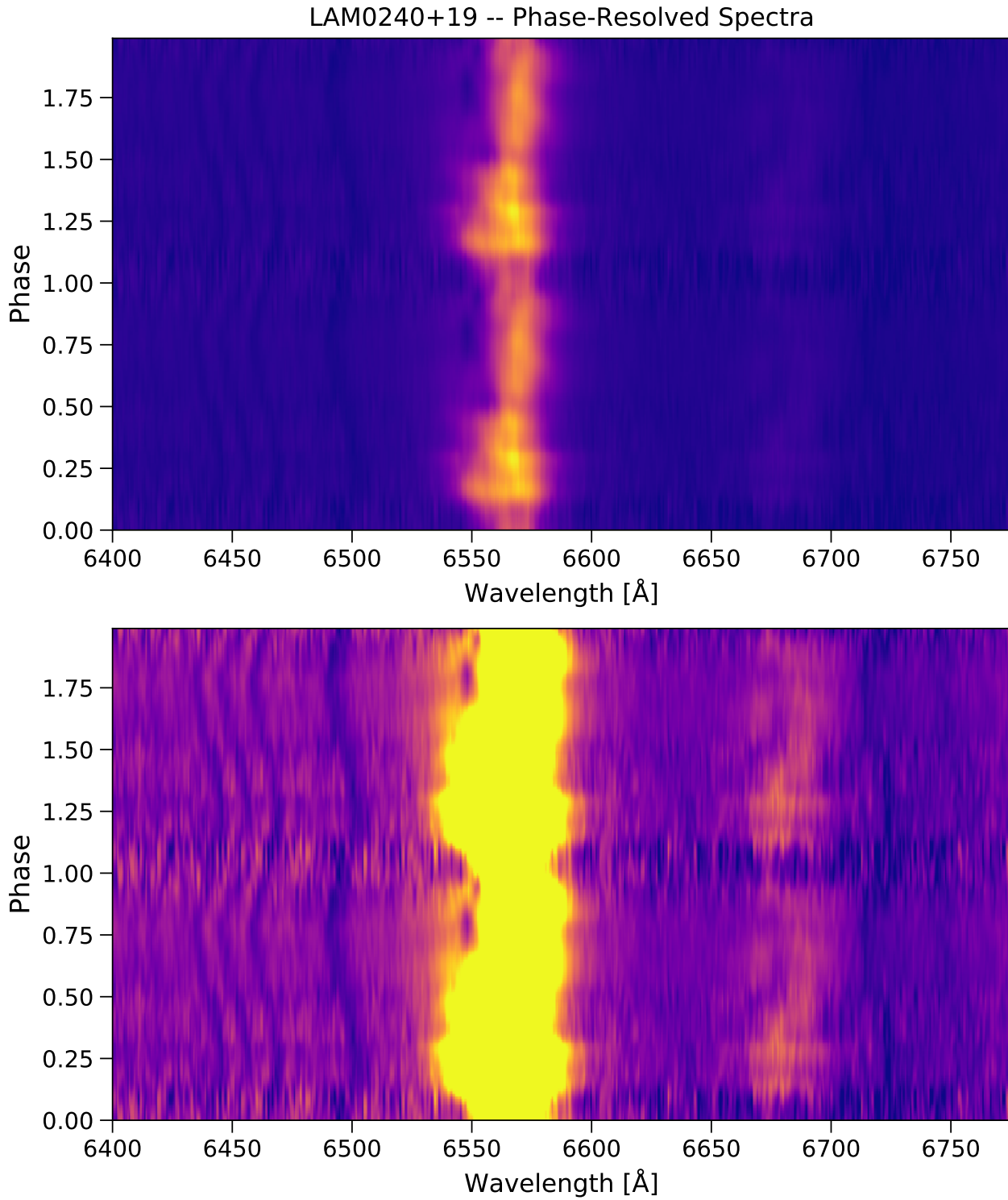
the phase at which the secondary would eclipse the accreting object if the binary inclination were higher. The folded Catalina magnitudes (Fig. 1) show a pattern of two maxima and two unequal minima per orbit, evidently so-called ellipsoidal variation caused by the tidal distortion of the secondary star. The deeper of the two minima occurs near phase  $\phi = 0.5$ , as expected from the deeper gravity darkening on the side facing the L1 point. The numerous brighter points in the CRTS light curve suggest short-lived flares of up to about 1 mag.

Fig. 3 shows a synthetic “trailed” spectrogram. Each line in the image represents the spectrum at a phase in the orbit, and is formed from an average of spectra taken near the fiducial phase, weighted by a Gaussian in phase. The spectra were continuum- divided (rectified) before averaging. Horizontally-extended noisy patches are poorly-covered intervals of orbital phase. The absorption lines of the late-type star show an obvious velocity modulation, but the emission lines behave in a complicated fashion that does not appear repeatable with phase.

Fig. 4 shows time-series photometry from five successive nights in 2019 December. They show intermittent rapid flaring by almost 1 magnitude, on timescales as short as  $\sim 1$  min in the first light curve, and also flickering on longer time scales. There is no obvious correlation with orbital phase in this short data set, though the CRTS data suggest they are more common near quadrature than near conjunction. The behavior is reminiscent of magnetic CVs, but nearly all magnetic CVs show strong He II emission, which is absent here.

On three of the five nights for which we have photometry, we obtained some spectra that were simultaneous. The time intervals covered are also shown in Fig. 4. Fig. 5 shows averages of five spectra taken 2019 Dec. 16, when the simultaneous photometry showed the source flaring, and four spectra taken Dec. 15 and 19, when flares were not occurring. During the flaring interval, H $\alpha$  emission line grew stronger and broader, and developed a blueshifted absorption feature at  $\sim -420$  km s<sup>-1</sup>. H $\beta$  (not shown) behaved similarly. The inconsistent emission-line velocities noted earlier, and the chaotic appearance of the emission lines in Fig. 3, appear to be associated with flaring.

Unlike nearly all newly-discovered CVs, LAMOST 0240+19 does not naturally fall into one of the well-populated CV subclasses. It is evidently not a dwarf nova, nor is it a polar (AM Her star) or intermediate polar (DQ Her star), nor does it resemble the UX Uma or SW Sex-type novalikes. However, with the limited information we have available, it is an excellent match for an object that has until now been unique – AE Aquarii. In what follows we summarize what is known about AE Aqr, and point out the apparent family resemblance.



**Figure 3.** Spectra of LAM 0240+19 near  $H\alpha$ , as a function of phase. In the upper panel, the colormap is set to show details of the  $H\alpha$  line, and in the lower panel it is set to show the absorption features and the He I  $\lambda 6678$  emission. The  $H\alpha$  profile shows irregular variations because all spectra are included, including those taken during flares.



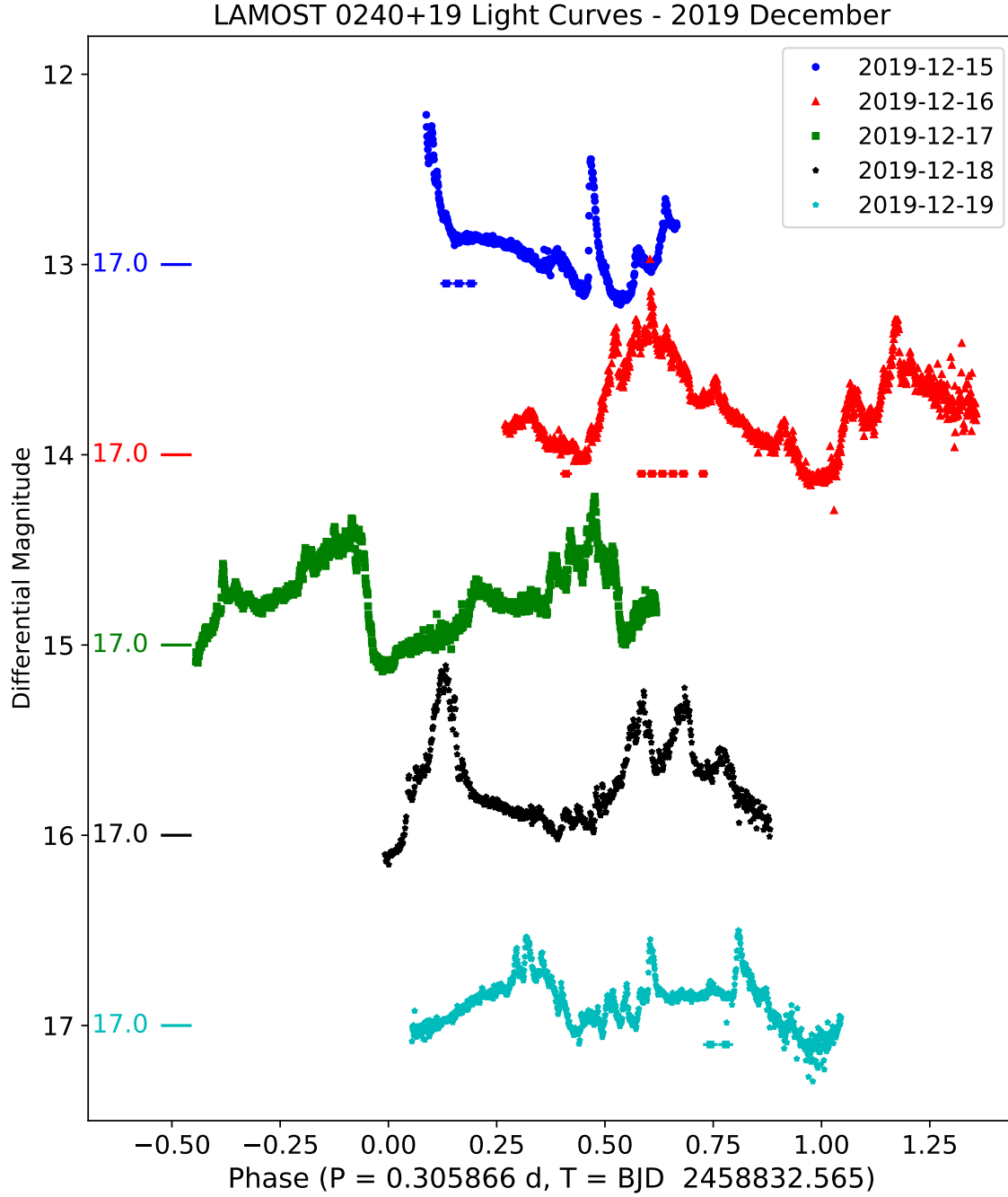


**Figure 4.** Light curves of LAMOST 0240+19 from five successive nights in 2019 December, plotted against orbital phase. The zero points for different nights are offset by 1.0 mag as indicated by the color-coded tick marks. The white-light differential magnitudes have been adjusted to rough  $V$  magnitudes using the comparison star, near  $\alpha_{\text{ICRS}} = 2:40:52.330$ ,  $\delta_{\text{ICRS}} = +19:53:00.74$ , for which the APASS catalog (Henden et al. 2016) gives  $V = 15.91$ . Exposures were 20 s, with a cycle time of 23.3 s, except for 2019-12-18 UT, for which the corresponding figures were 30 s and 33 s. Also shown are the times (orbital phases) of spectroscopic exposures taken simultaneously; these are plotted as color-coded squares at the 17.1-magnitude level for each night. The short horizontal error bars indicate the duration of each exposure.

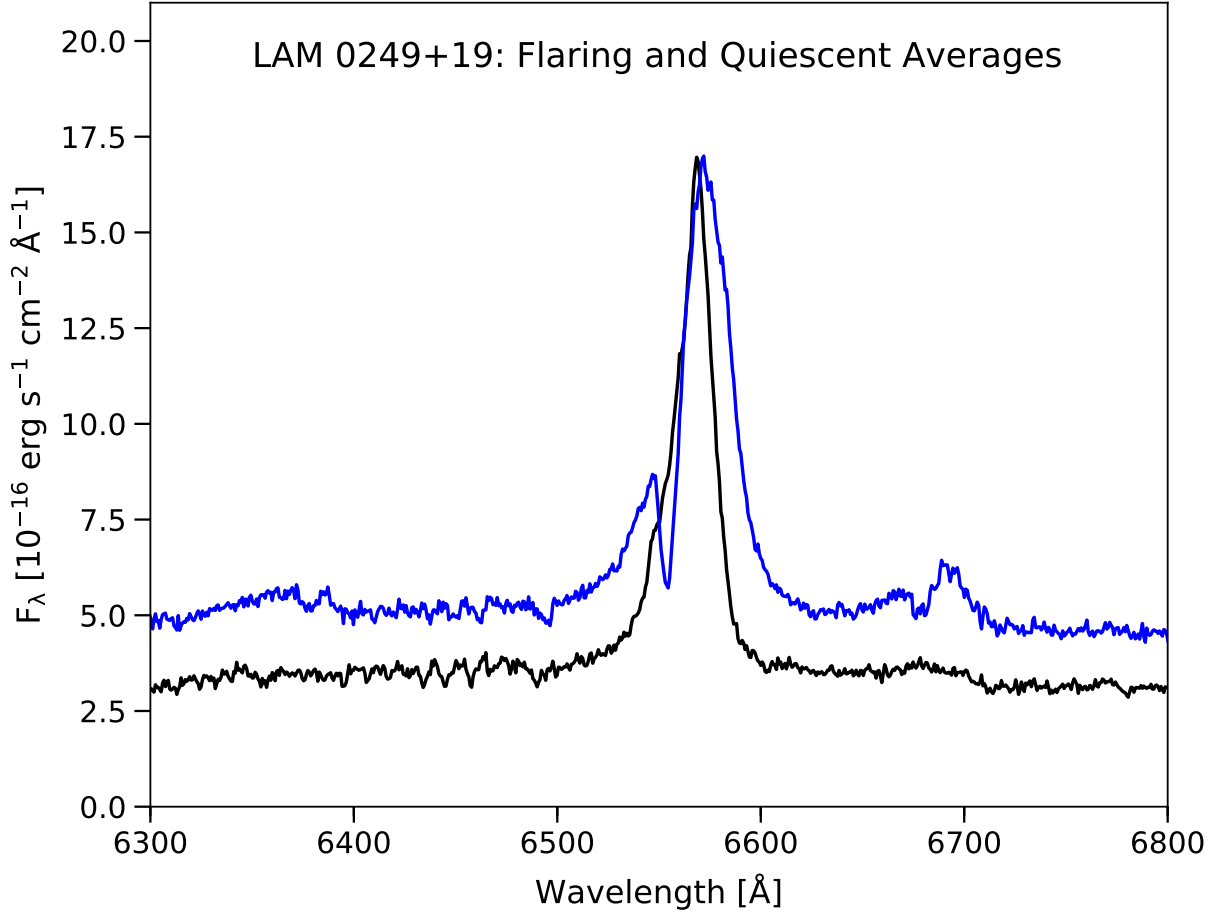


**Figure 5.** Averages of spectra taken during and outside of flaring intervals in the region of  $H\alpha$ . As these were taken, the comparison star used for the photometry appeared reasonably steady, and the setup exposures indicated similar seeing throughout, so the flux difference between the flaring (upper, blue trace) and non-flaring (lower, black trace) is probably real.

AE Aqr was among the first CVs recognized as a binary star (Joy 1943); it is bright, with a mean  $G = 10.95$  in the Gaia DR2. Its brightness is largely caused by its proximity (91 pc), which puts it in the  $< 150$  pc volume-limited sample assembled by Pala et al. (2020). It is evidently a magnetic CV, but with unusual features.

Like LAMOST 0240+19, AE Aqr is a longer-period CV with a prominent secondary star contribution already noted by Joy (1943). Its orbital period, 9.98 hr, is not dissimilar to the 7.34-hr period of LAMOST 0240+19. As expected at this somewhat longer orbital period, its secondary star (K5; Robinson et al. 1991) is somewhat warmer than the M1.5 secondary in LAMOST 0240+19. Also like LAMOST 0240+19, the spectrum of AE Aqr does not show appreciable He II emission, and the He I lines are also not strong for a CV (Williams 1983; Echevarría et al. 1989). While the emission lines in AE Aqr can vary rather smoothly in velocity (Robinson et al. 1991), they often show dramatic and irregular variation (Chincarini & Walker 1981; Reinsch & Beuermann 1994; Welsh et al. 1998).

The most striking similarity between AE Aqr and LAMOST 0240+19 is that their light curves both show distinctive, irregular flaring on time scales of minutes. Nearly all CVs flicker, but flares of this kind are unusual except among magnetic CVs in high states. The literature offers many examples of flaring light curves of AE Aqr (e.g. Chincarini & Walker 1981; Welsh et al. 1998; Watson et al. 2006). The resemblance between these and Fig. 4 is striking.

At high time resolution, the light curve of AE Aqr shows a coherent 33-s oscillation (Patterson 1979), which is thought to be the rotation period of a magnetized white dwarf. This is the shortest known white dwarf rotation period. The unique features of AE Aqr are explained by a *propeller effect* – the magnetic field of the rapidly spinning white dwarf expels most of the mass transferred from the secondary, with only a rather small fraction ultimately accreting onto the white dwarf (Eracleous & Horne 1996; Wynn et al. 1997).

If high time resolution photometry were to yield a short-period (tens of seconds) coherent pulsation in LAMOST 0240+19, its kinship to AE Aqr would be conclusively proven. Unfortunately, the cadence of our photometry – 23 sec in 2019 December and 30 sec for a short segment in 2020 January – is too slow to show this. Searches at very high frequencies show only aliases of the ellipsoidal modulation. When new observations become possible, a search for pulsations in the relevant period range could be very rewarding. LAMOST 0240+19 is much fainter than AE Aqr, and the pulsations in AE Aqr are not always obvious, but the observational task is eased by the coherence of white dwarf rotation over long time spans.

### 3.2. LAMOST J033940.98+414805.7

The mean spectrum of this object (Fig. 6, top panel) is typical for a novalike CV, with a strong, blue continuum and emission lines of hydrogen and He I. Weak emission is visible at He II  $\lambda 4686$  and the C III-N III blend at  $\lambda 4640$ . Its position is not covered by the CRTS.

We measured radial velocities of the H $\alpha$  emission using for the convolution function the derivative of a Gaussian, optimized for a line with a 900 km s<sup>-1</sup> FWHM. The middle panel of Fig. 6 shows the velocities folded on a period of 3.543(5) hr, which is determined without ambiguity. Many CVs in this period range are SW Sex stars (Rodríguez-Gil et al. 2007; Thorstensen et al. 1991), and the mean spectrum does appear similar to stars of this class; however, the phase-averaged spectrogram shown in the lower panel of Fig. 6 does not show the phase-dependent absorption often present in SW Sex stars. The appearance of phase-dependent absorption probably requires an orbital inclination not too far from edge-on. The H $\alpha$  line in the phased spectrogram appears to have two components, one of them fairly narrow and the other broader. The narrower component appears to be the one measured by the convolution function; the broad component shows little or no motion on the orbital period. The narrower component may arise from the bright spot formed where the mass-transfer stream strikes the accretion disk; if so, most of its velocity variation would be from the rotation of the disk rather than the orbital motion of the white dwarf.

In summary, this appears to be a fairly typical, but previously unrecognized, novalike variable.

### 3.3. LAMOST J035913.61+405035.0

The top panel of Fig. 7 shows the CRTS DR2 light curve of this object, which appears to have spent most of 2007-2009 in a relatively bright state around 16th magnitude, and then faded to a more typical state near 17th, with occasional outbursts to the brighter state. The light curve is consistent with a dwarf nova; the persistent high state is characteristic of the Z Cam subclass. The total range of variation,  $\sim 2.5$  mag, is rather low for a dwarf nova.

Our mean spectrum (Fig. 8, top panel) appears typical for a dwarf nova near minimum light. An early M star contributes to the continuum, as can be seen from the absorption bands longward of 6000 Å. We estimate the spectral type as M1  $\pm 1$  subclass, and that the secondary star’s contribution is equivalent to  $V = 20.3$ , with an uncertainty of  $\sim 0.5$  mag. A period search of the H $\alpha$  emission-line velocities (Fig. 8) shows an unambiguous period of 5.494(17) hr. We attempted to measure cross-correlation velocities of the M dwarf, but due to the faintness of its contribution and sometimes poor signal-to-noise, only some of our spectra gave usable results, and those were rather imprecise. The lower panel of Fig. 8 shows both the emission and cross-correlation velocities folded on the provisional eclipse ephemeris (discussed below).

The target acquisition images mostly showed the source near  $g = 18.5$  in 2019 December, but four images showed it distinctly fainter at  $g > 19.5$  (Fig. 7, middle panel). Faint states occurred on three different nights, and always occurred near the same orbital phase. Furthermore, the phase of these faint states corresponds approximately to blue-to-red crossing of the M-dwarf velocity, which is the inferior conjunction of the red dwarf. The faint state is evidently an eclipse.

We attempted to refine the ephemeris by folding the CRTS data on a range of finely-spaced periods near the period found from the H $\alpha$  velocities. We found several refined periods in which the faint CRTS points cluster in phase; the best-fitting of these gives a provisional eclipse ephemeris

$$\text{BJD eclipse} = 2458832.880 + 0.228344E, \quad [\text{provisional}], \quad (3)$$

where  $E$  is an integer cycle count and the quantities are uncertain by one or two in the last digits shown. The lower panel of Fig. 7 shows the CRTS data folded on the provisional ephemeris.

The provisional ephemeris should be easy to test and refine with precise eclipse timings from time-series photometry resolving the ingress and egress. If more accurate radial velocities of the secondary star can also be obtained, a good white-dwarf mass estimate should be within reach.

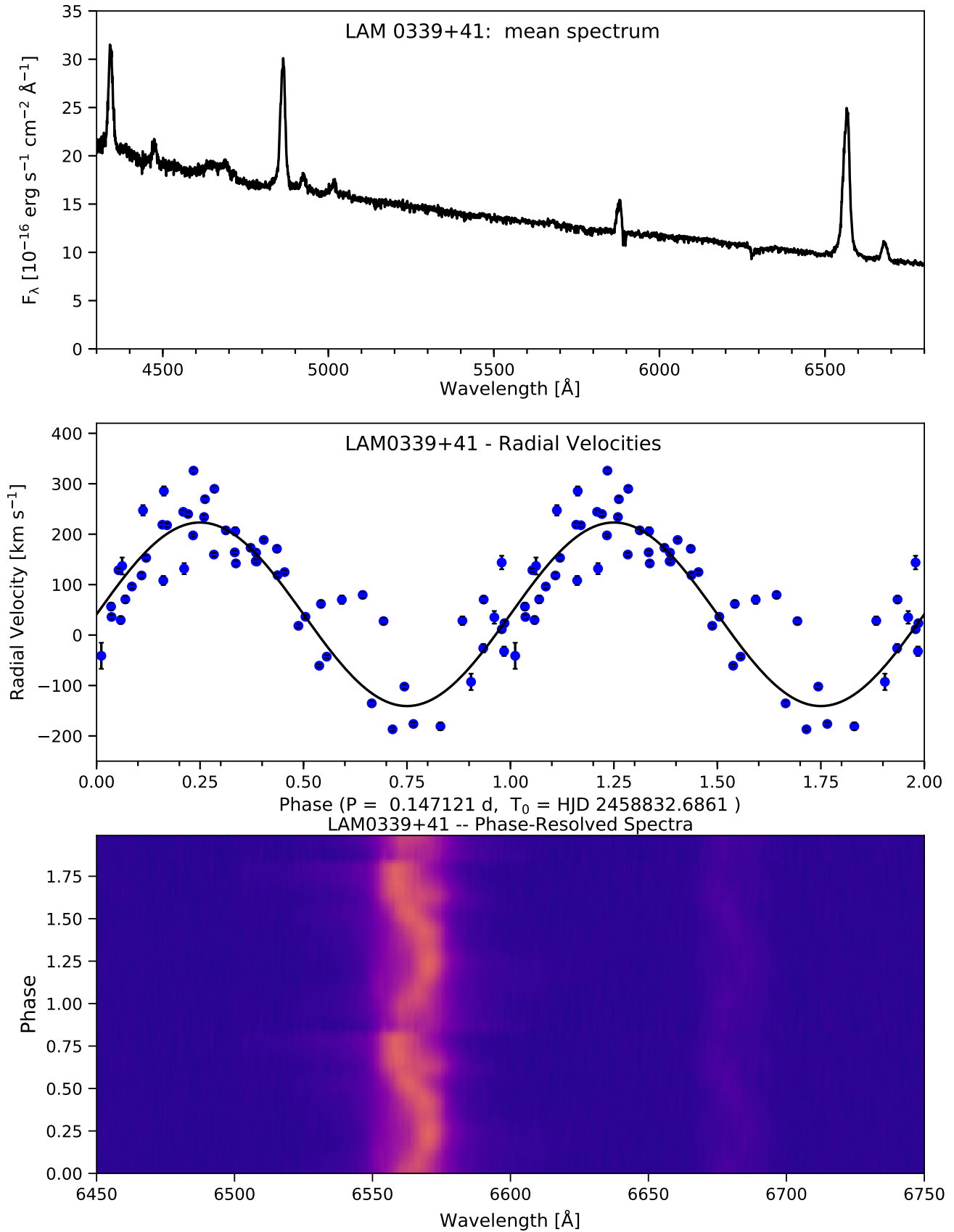


**Figure 6.** Upper panel: The mean spectrum of LAMOST 0339+41. Middle panel: Radial velocities of the narrower component of the H $\alpha$  emission line, folded on the ephemeris shown. Lower panel: A portion of the rectified, phase-averaged spectrogram.

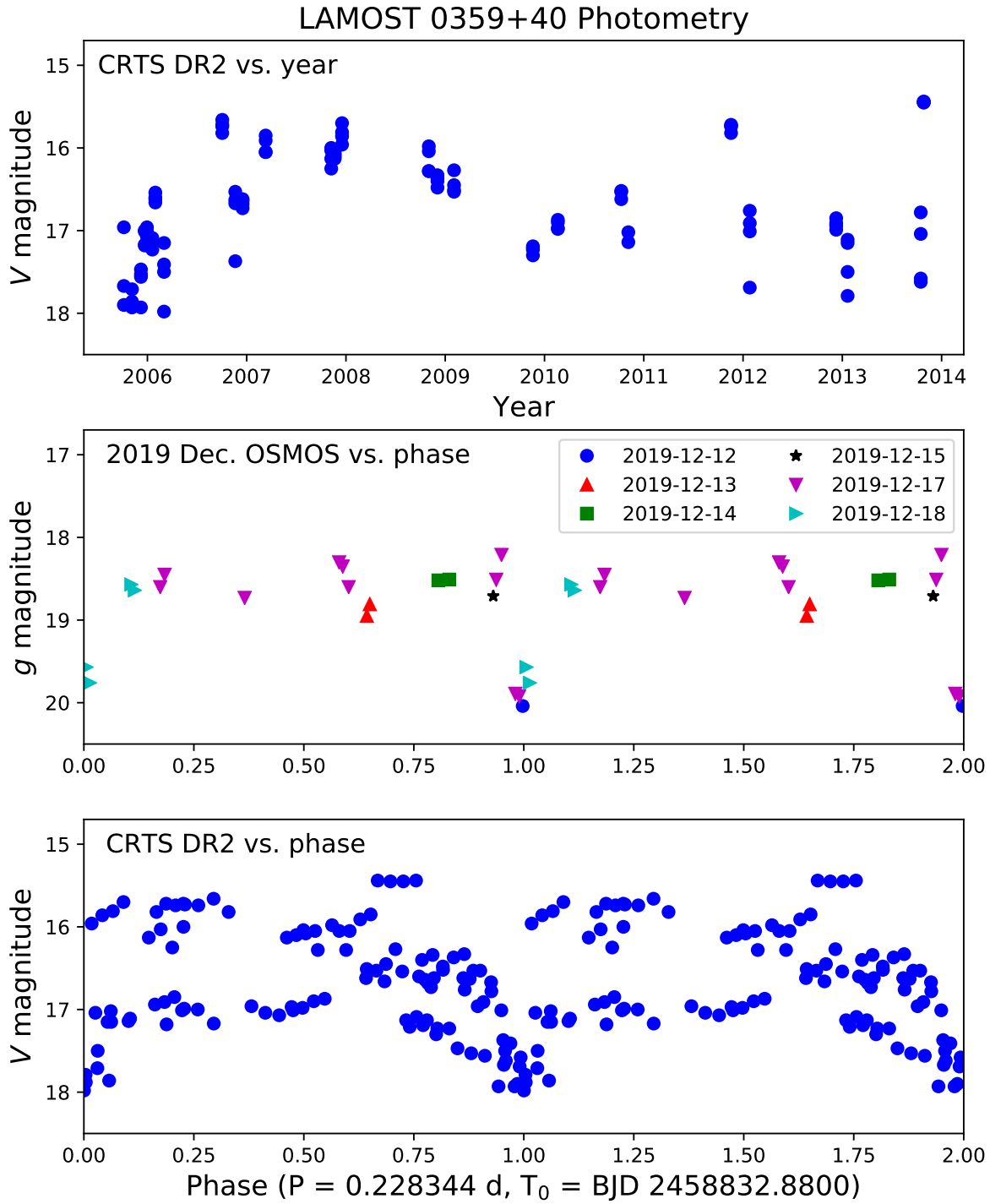


**Figure 7.** Top panel: Archival photometry of LAM 0359+40 from the CRTS DR2. Middle panel: Magnitudes from target acquisition images taken 2019 Dec., folded on the provisional eclipse ephemeris. Lower panel: The same data as the top panel folded on the provisional ephemeris.

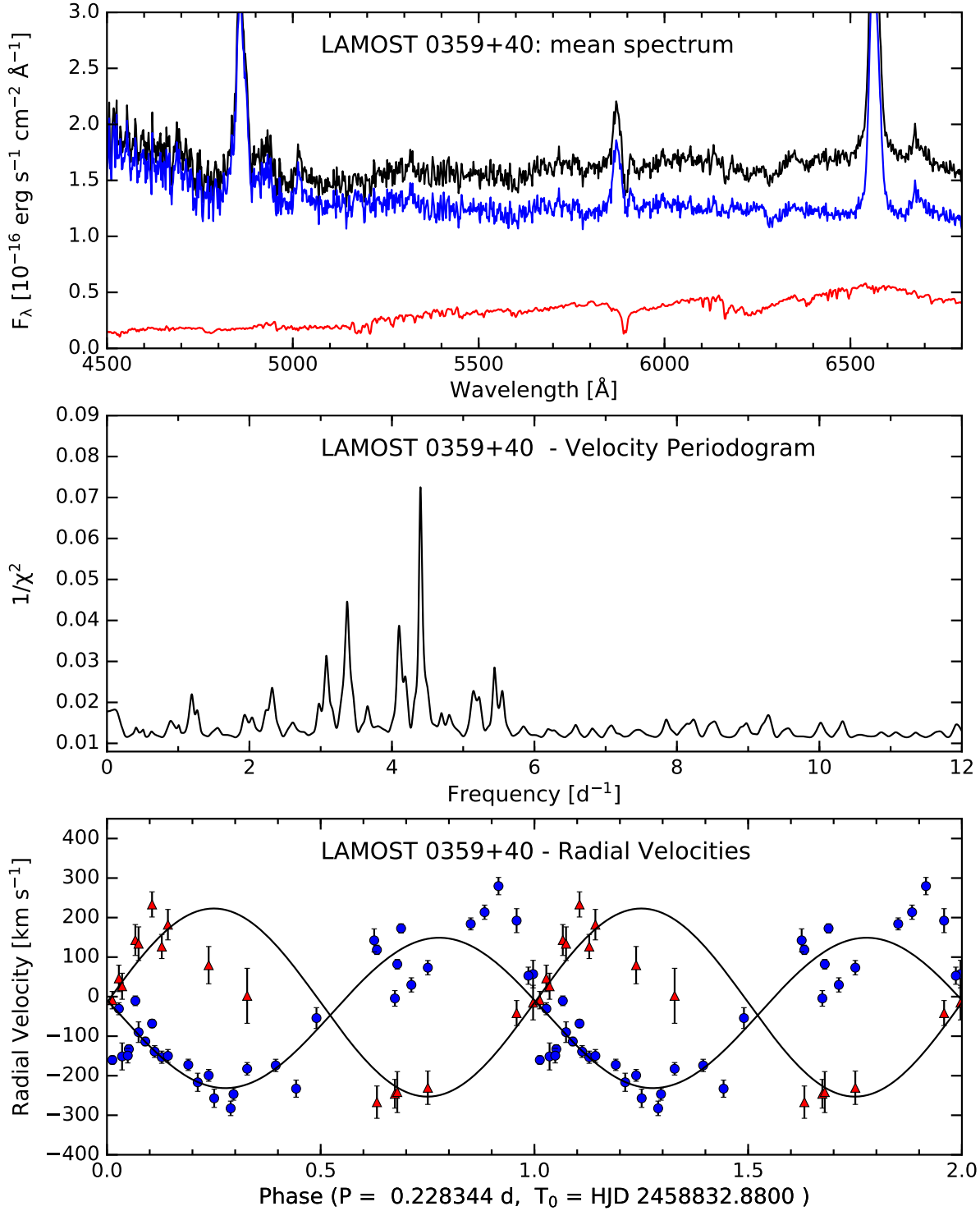


**Figure 8.** Top panel: The top trace (black) shows the mean spectrum from 2019 December. The lower trace (red) is a spectrum of the M1.0 star Gliese 514, scaled to  $V = 20.3$  mag. The middle trace (red) is the difference between these two. Middle panel: Periodogram of the  $H\alpha$  emission velocities. Lower panel: Radial velocities of the emission (blue) and absorption (red), folded on the provisional ephemeris (see text). The best-fitting sinusoids are overplotted; in the fit shown for the absorption, the phase was fixed to that of the eclipse ephemeris.

## 3.4. LAMOST J090150.09+375444.3

This object’s LAMOST spectrum (Hou et al. 2020) shows strong, rather narrow Balmer and HeI emission lines, and He II  $\lambda 4686$  about 2/3 of the strength of H $\beta$ , which is usually a sign of magnetic activity. A sizable late-type star contribution is also visible in the continuum, with the strong blend and continuum break near 5180 Å characteristic of late K stars, and relatively weak molecular absorption bands typical of early M stars. It appears in the list of periodic variables found in CRTS; Drake et al. (2014) list  $P = 0.2833870$  d. The top panel of Fig. 9 shows the CRTS data; the bottom panel shows the same data folded on the period, showing the double-humped signature of ellipsoidal modulation, with a full amplitude of a bit over 0.2 magnitude. No substantial outbursts are observed. The variation in the  $g$  magnitudes from the target-acquisition images (lower panel) appears consistent with the ellipsoidal modulation in the CRTS data.

Our mean spectrum (Top panel of Fig. 10) is significantly different from the LAMOST spectrum, in that He II  $\lambda 4686$  is not detected, and the He I lines are also less prominent. The late-type contribution is still present. We tried our standard procedure of scaling and subtracting late-type spectra from this, but this did not give a satisfactory spectral decomposition. The strong absorption in the  $\sim 5150$  Å region could only be subtracted with a strong late-K contribution, but this did not do a good job on the TiO bands toward the red. Early M-type spectra fit the TiO bands well, but did not match the shorter-wavelength features.

Both the H $\alpha$  emission and the absorption velocities varied smoothly with orbital phase, and both data sets independently yielded periods consistent with the more precise Drake et al. (2014) period. The blue-to-red crossing of the absorption velocities corresponds to inferior conjunction of the late-type star, so we adopt this as phase zero for the ephemeris

$$\text{BJD inferior conjunction} = 2458836.152(2) + 0.2833870E. \quad (4)$$

The lower two panels of Fig. 10 show that the H $\alpha$  emission velocities move *in phase* with the absorption, with a somewhat smaller velocity amplitude. It appears to arise from the side of the secondary star that faces the primary. Emission lines from the secondary are seen in some CVs, but seldom dominate the emission.

Several scenarios could explain this unusual behavior. In all the scenarios, the rate of accretion onto the primary must have been low enough during our observations so that we do not see an accretion disk or column.

One explanation is that the primary star emits enough ionizing radiation to excite fluorescent emission on the facing side of the secondary. However, if this mechanism dominates the emission, and the flux of ionizing radiation is steady and isotropic, the changing aspect of the illuminated face should cause the emission line strength to vary smoothly and symmetrically with orbital phase; the detached WD-dM binary FS Cet (Feige 24; Thorstensen et al. 1978) remains an excellent example. Fig. 11 shows the H $\alpha$  emission line strength as a function of orbital phase. The illuminated-face hypothesis predicts maximum strength at phase 0.5 (red-to-blue crossing for the secondary stars’s velocities), and while there is a tendency for the line to be stronger around phase 0.5, the variation is not as smooth and symmetric as expected.

Alternatively, the magnetic activity of the secondary may be strong. CV secondary stars are forced to rotate rapidly because they are tidally locked to the orbit. The rapid rotation is thought to enhance their magnetic activity, which in turn should produce chromospheric emission. In most CV spectra the accretion makes this emission inconspicuous, but it could emerge when the accretion turns off. The chromospheric hypothesis does not naturally explain why the velocity amplitude of the emission is smaller than that of the absorption; explaining this requires an *ad hoc* assumption that the emission arises mostly on the side facing the primary.

The velocity modulation does prove that LAMOST 0901+37 is a close binary system, but our spectra alone do not demonstrate that it is a CV. However, the strong He II  $\lambda 4686$  in the Hou et al. (2020) spectrum does show conclusively that the system goes into more active states, and a strong  $\lambda 4686$  line often indicates a magnetic CV. These sometimes drop into low states in which the accretion practically stops. The low states can last for years (see, e.g., EF Eri; Szkody et al. 2010). Another class of stars in which mass transfer essentially shuts off are the VY Sculptoris stars, a class of novalikes that strongly overlaps SW Sex stars. VY Scl stars can spend long intervals in low states, but typically have periods in the 3-4 hr range (Rodríguez-Gil et al. 2020), much shorter than here.

LAMOST 0901+37 may be similar to V405 Peg (Thorstensen et al. 2009; Schwöpe et al. 2014), which has a slightly shorter period but also has a varying emission spectrum. In V405 Peg, the H $\alpha$  line in the strong-line state varies in velocity roughly in antiphase to the absorption-line spectrum, while in the weak-line state H $\alpha$  is narrower and its motion small and ill-defined. A significant difference between the two systems is that V405 Peg is a fairly strong X-ray source (Rosat Bright Source 1955), while none of the X-ray source catalogs on Vizier list any sources near ( $< 2$  arcmin)

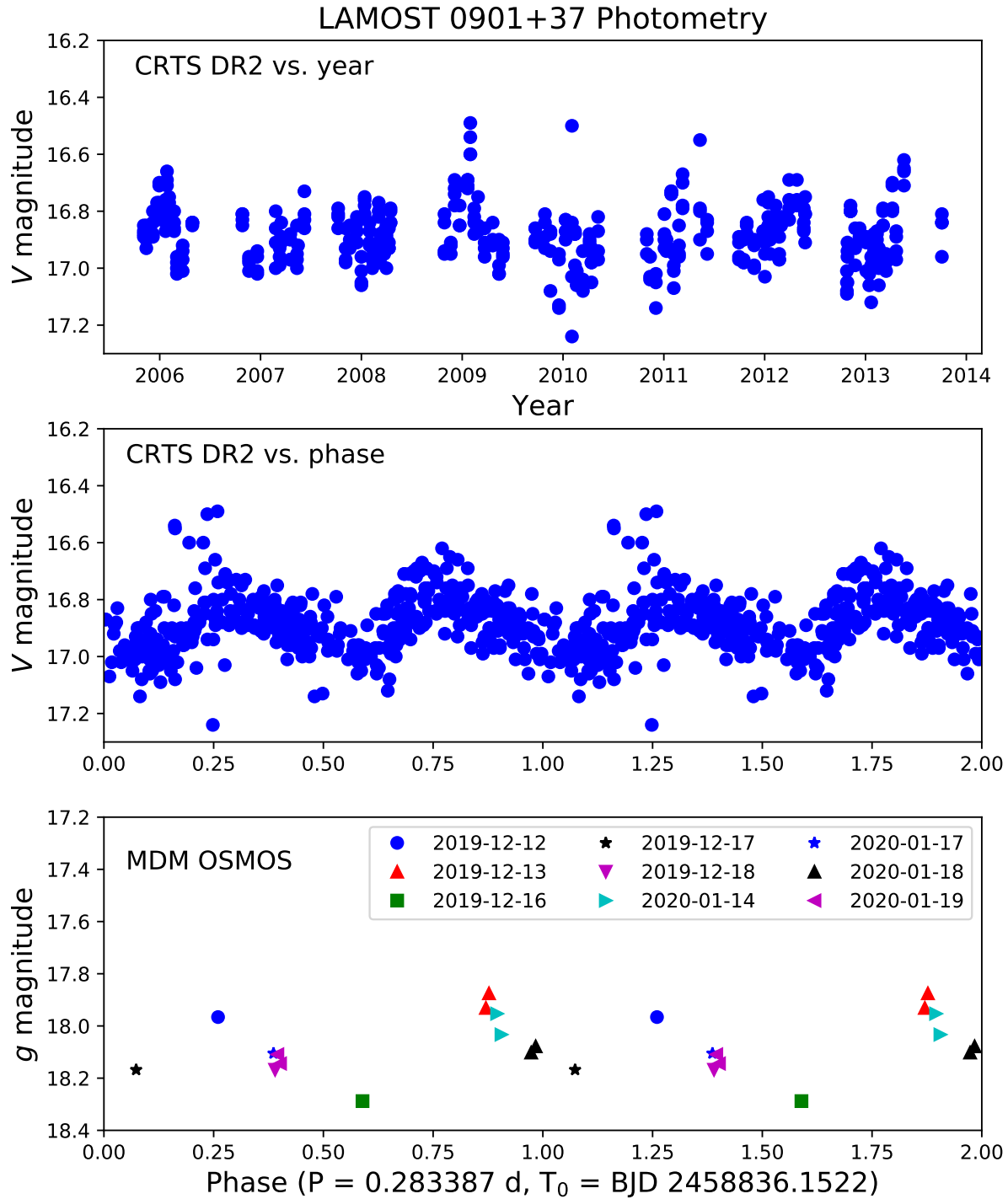


**Figure 9.** Top panel: Archival CRTS magnitudes of LAMOST 0901+37 plotted as a function of time. Middle panel: The same data plotted as a function of phase. The period is from [Drake et al. \(2014\)](#), and the epoch chosen to match the blue-to-red crossing of the absorption line radial velocities. Lower panel:  $g$  magnitudes from the OSMOS target acquisition images, plotted against phase.



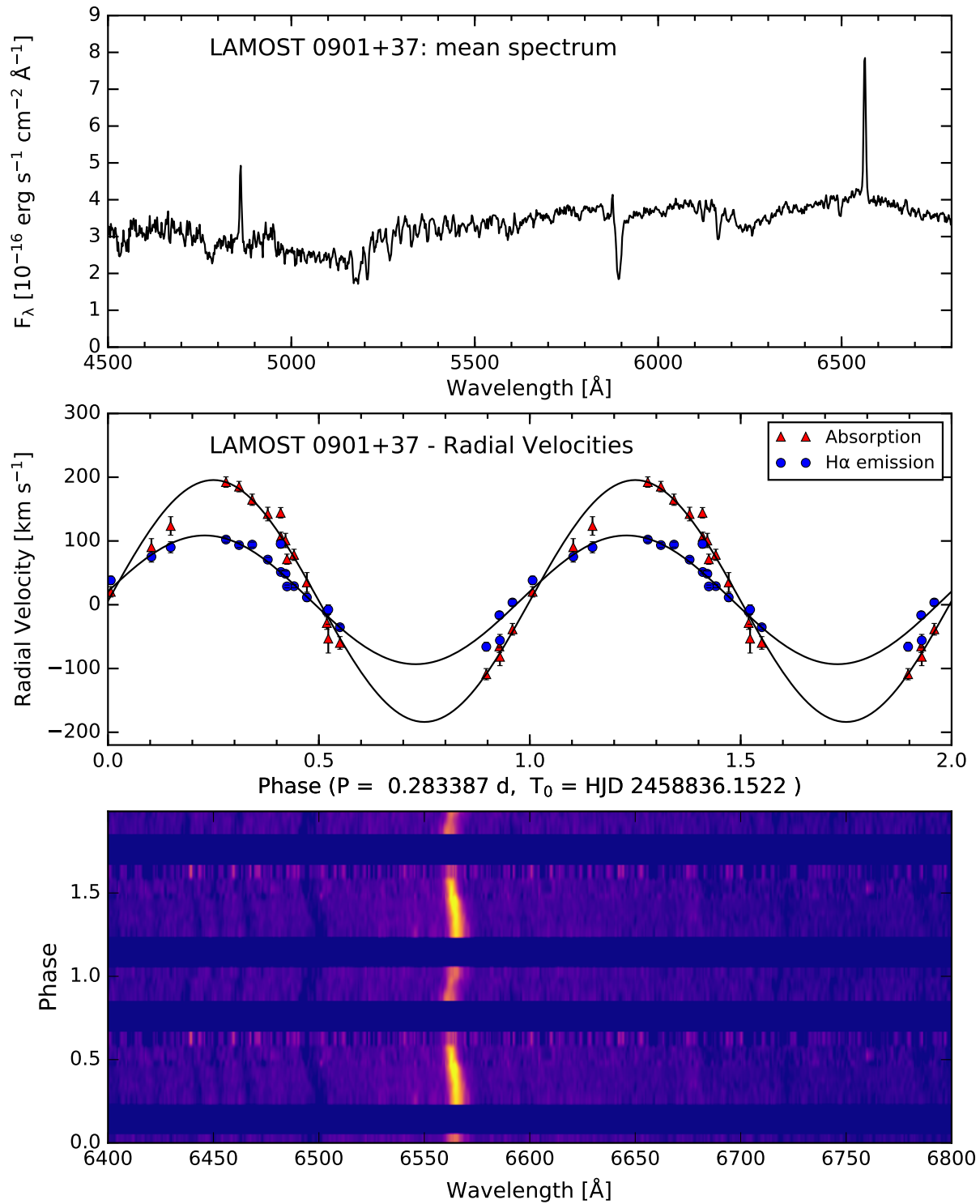


**Figure 10.** Top panel: Mean MDM spectrum of LAMOST 0901+37, from 2019 December and January. Middle panel: Radial velocities of the H $\alpha$  emission (blue) and late-type absorption features (red) plotted as a function of phase. Lower panel: Phase-averaged spectra in the vicinity of H $\alpha$ . The blank horizontal spaces correspond to phases that were not covered.

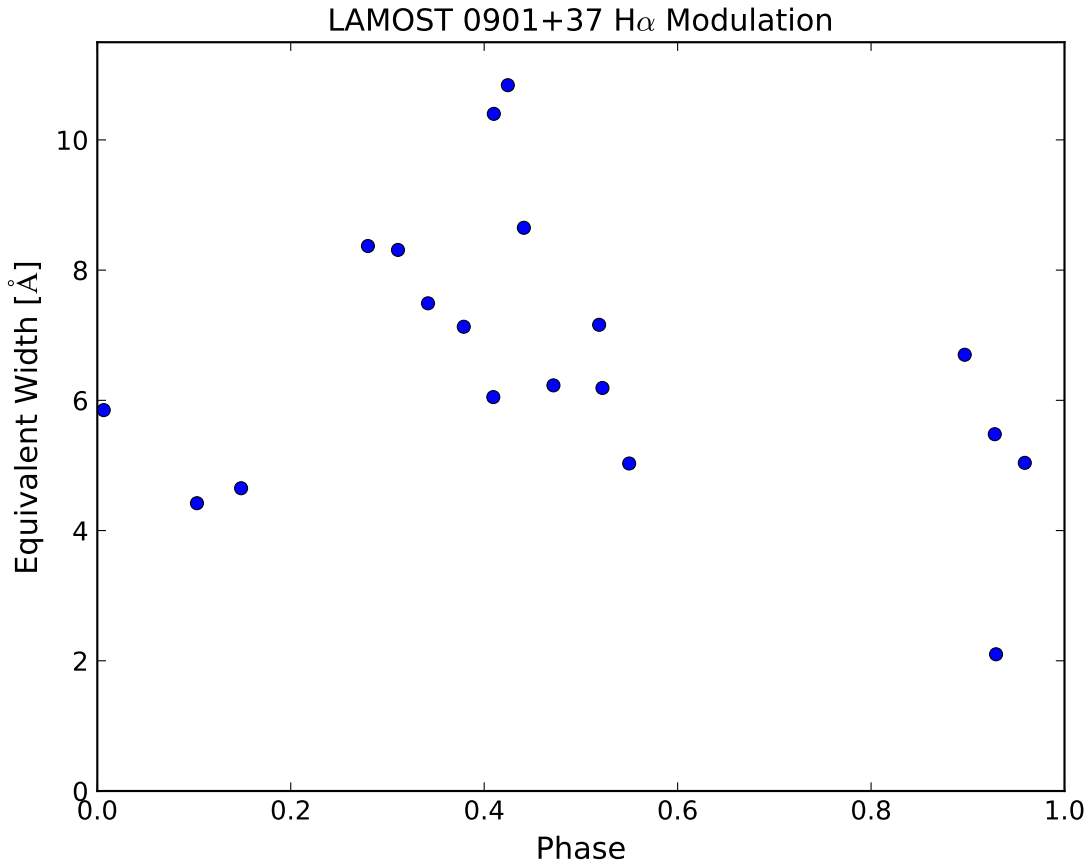


**Figure 11.** Equivalent width of the H $\alpha$  emission in LAMOST 0901+37 as a function of orbital phase.

LAMOST 0901+37. At 525 pc, LAMOST 0901+37 is almost exactly 3 times as distant as V405 Peg (173 pc in Gaia DR2<sup>3</sup>, so if it were the same X-ray luminosity as V405 Peg it would be 9 times fainter. The ROSAT all sky bright source catalog (Voges et al. 1999) lists V405 Peg at 0.21 counts s<sup>-1</sup> and includes sources brighter than 0.05 counts s<sup>-1</sup>, so it seems possible that LAMOST 0901+37 has been missed because of distance. It could also have a low duty cycle.

### 3.5. LAMOST J204305.95+341340.6

Margoni & Stagni (1984) found the variability of this object in a Schmidt survey of a low-Galactic-latitude field. They list its magnitude range as  $15.0 < V < 15.4$  and  $16.0 < B < 16.9$ , without further detail. Skiff (1997) published improved coordinates. Its celestial location is not covered by the CRTS.

The LAMOST spectrum (Hou et al. 2020) has a strong blue continuum with broad Balmer emission lines and relatively weak He I emission; however, He II  $\lambda 4686$  and the C III-N III blend around  $\lambda 4340$  are both strong, around half the strength of H $\beta$ . The mean MDM spectrum (top panel of Fig. 12) is similar to the LAMOST spectrum. The target acquisition images have  $15.39 < g < 15.71$ , indicating that the photometric state was similar to that in which Margoni & Stagni (1984) found it.

A search of the H $\alpha$  velocities yields a best-fit period of 2.586(3) hr, but because the object was only observable for a few hours per night, a 2.899(3) hr period also fits well; these two periods differ in frequency by almost exactly 1 cycle d<sup>-1</sup>. The middle panel of Fig. 12 shows the velocities folded on the 2.586(3) hr period. While the daily cycle count remains undetermined, the system’s period evidently lies in the so-called 2-3 hour “gap” in the CV period distribution.

<sup>3</sup> Thorstensen et al. (2009) estimated the distance of V405 Peg to be 149(+26, -20) pc based mostly on ground-based parallax measurements.

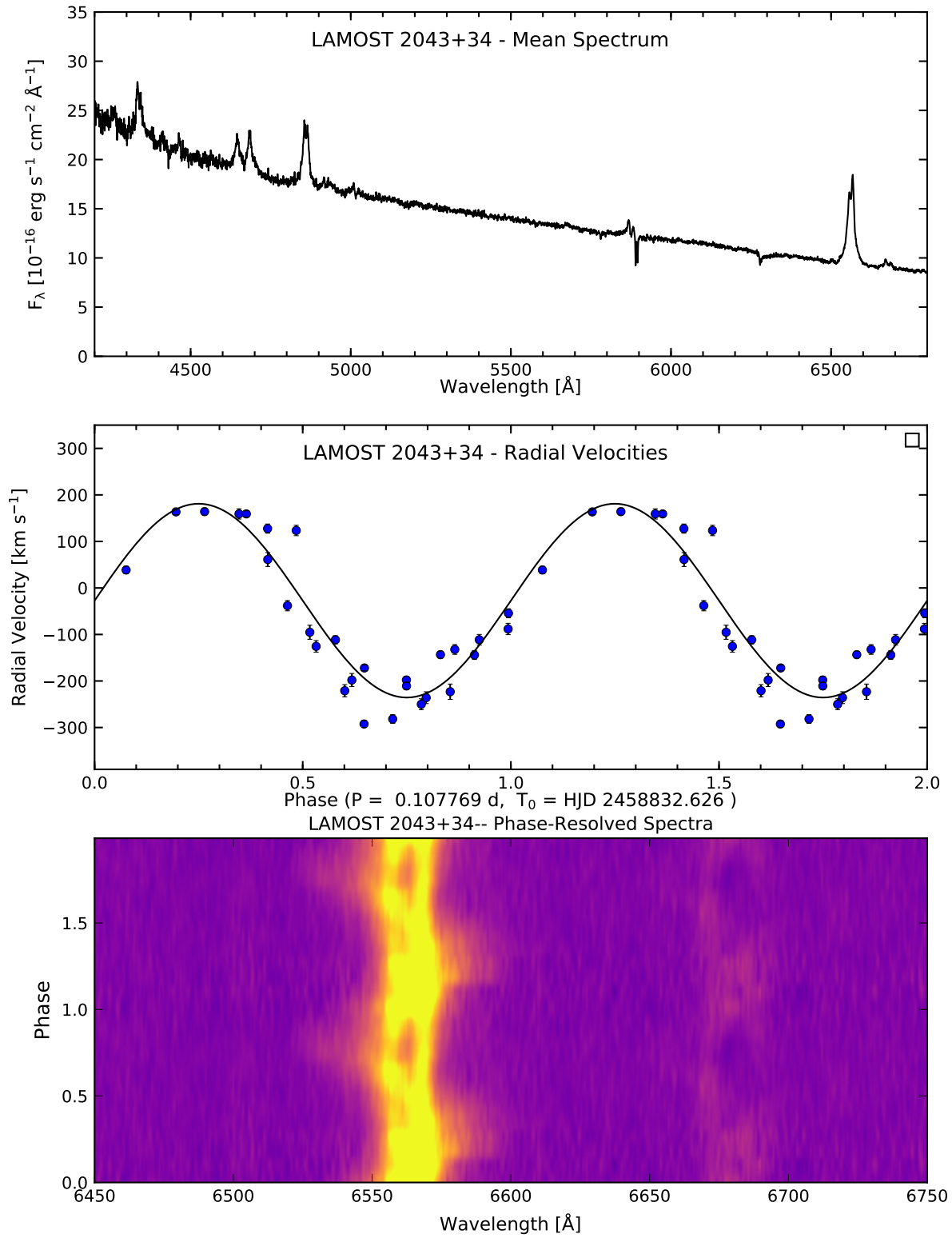


**Figure 12.** Top panel: Mean spectrum of LAMOST 2043+34 from 2019 December. Middle panel: Radial velocities of H $\alpha$  folded on the best-fitting period of 2.586 hr; an alias period at 2.899 hr fits nearly as well. Lower panel: Phase-averaged spectra in vicinity of H $\alpha$  and He I  $\lambda 6678$ .

The lower panel of Fig. 12 shows the phase averaged spectra near  $H\alpha$ . The central part of the line profile has two distinct peaks separated by  $\sim 550 \text{ km s}^{-1}$ . The peaks vary relatively little in velocity; by marking the peaks on an expanded display of the data in Fig. 12, we estimate  $K \sim 60 \text{ km s}^{-1}$  for the peaks' motion. The most striking feature of the line profile is a much wider wing that swings from one side of the line to the other over the orbit. At its maximum red and blue shifts, near phases 0.3 and 0.8 in the figure, it extends  $\sim 2000 \text{ km s}^{-1}$  from rest. The pattern strikingly resembles the line profile variation in V795 Her, for which Casares et al. (1996) present time-series spectroscopy and a thorough analysis. V795 Her is a novalike variable with  $P_{\text{orb}} = 2.597 \text{ hr}$ , very close to the 2.586 hr best-fit period for LAMOST 2043+34. The similarity extends to the two systems' luminosities as well; Gaia DR2 list 589(13) pc and  $G = 13.08$  for V795 Her, and Green et al. (2019) give  $E(g - r) = 0.04(2) \text{ mag}$ . This results in  $M_G = 4.1$  for V795 Her, while the same calculation yields  $M_G = 4.3$  for LAMOST 2043+34 (Table 1). LAMOST 2043+34 and V795 Her appear to be virtually identical.

#### 4. DISCUSSION

These results underscore how easy it can be for interesting objects to go unnoticed, if the usual search criteria do not include them. While three of the five stars studied here had previously been noted as variable, none have a large range of variation, and none had been recognized as a CV. Even so, all of the stars prove to be interesting and for several, further work should yield significant improvements. Our most surprising result is that LAMOST 0240+19 appears to be the long-lost twin of AE Aqr; this cries out for fast photometry sufficient to resolve pulsations with periods down to a few seconds. LAMOST 0359+40 has a detectable secondary star and an eclipse, and may be favorable for a white-dwarf mass determination; this will require proper time-series photometry to resolve the eclipses and sharpen the ephemeris, and better velocities of the secondary. LAMOST 0901+37 appears to have dipped into a low state in which accretion has dropped to negligible levels; it should be watched for a return to the high state seen in its discovery spectrum. LAMOST 2043+34 is in the period gap, and appears identical to V795 Her. LAMOST 0339+41 appears to be a low-inclination SW Sex star; these are often also VY Scl stars, so it may dive into low states in the future.

#### ACKNOWLEDGMENTS

The CSS survey, which is funded by the National Aeronautics and Space Administration under Grant No. NNG05GF22G issued through the Science Mission Directorate Near-Earth Objects Observations Program. The CRTS survey is supported by the U.S. National Science Foundation under grants AST-0909182 and AST-1313422. In addition, this research made use of the AAVSO Photometric All-Sky Survey (APASS), funded by the Robert Martin Ayers Sciences Fund and NSF AST-1412587.

We thank Dartmouth graduate students Kathryn Weil and especially Aylin Garcia-Soto for helping with the 2019 December observations, as well as Dartmouth undergraduates Catherine Slaughter, Chase Alverado-Anderson, and Piper Stacey for their company and assistance. Heartfelt thanks go to Claudia and Jay Weed for underwriting undergraduate observatory travel.

Finally, we would like to thank the Tohono O'odham Nation for leasing their mountaintop, so that we may explore the universe that surrounds us all.

#### REFERENCES

- Aungwerojwit, A., Gänsicke, B. T., Rodríguez-Gil, P., et al. 2006, *A&A*, 455, 659
- Buermann, K., Harrison, T. E., McArthur, B. E., Benedict, G. F., & Gänsicke, B. T. 2003, *A&A*, 412, 821
- Boeshaar, P. C. 1976, PhD thesis, Ohio State University, Columbus.
- Breedt, E., Gänsicke, B. T., Drake, A. J., et al. 2014, *MNRAS*, 443, 3174
- Carrasco, J. M., Evans, D. W., Montegriffo, P., et al. 2016, *A&A*, 595, A7
- Casares, J., Martínez-Pais, I. G., Marsh, T. R., Charles, P. A., & Lazaro, C. 1996, *MNRAS*, 278, 219
- Chincarini, G., & Walker, M. F. 1981, *A&A*, 104, 24
- Drake, A. J., Djorgovski, S. G., Mahabal, A., et al. 2009, *ApJ*, 696, 870
- Drake, A. J., Graham, M. J., Djorgovski, S. G., et al. 2014, *ApJS*, 213, 9
- Echevarría, J., Diego, F., Martínez, A., et al. 1989, *RMxAA*, 17, 15
- Eracleous, M., & Horne, K. 1996, *ApJ*, 471, 427

- Filippenko, A. V. 1982, *PASP*, 94, 715
- Gaia Collaboration, Prusti, T., de Bruijne, J. H. J., et al. 2016, *A&A*, 595, A1
- Gaia Collaboration, Brown, A. G. A., Vallenari, A., et al. 2018, *A&A*, 616, A1
- Goliasch, J., & Nelson, L. 2015, *ApJ*, 809, 80
- Green, G. M., Schlafly, E., Zucker, C., Speagle, J. S., & Finkbeiner, D. 2019, *ApJ*, 887, 93
- Green, R. F., Ferguson, D. H., Liebert, J., & Schmidt, M. 1982, *PASP*, 94, 560
- Henden, A. A., Templeton, M., Terrell, D., et al. 2016, VizieR Online Data Catalog, II/336
- Horne, K. 1986, *PASP*, 98, 609
- Hou, W., Luo, A. I., Li, Y.-B., & Qin, L. 2020, *AJ*, 159, 43
- Joy, A. H. 1943, *PASP*, 55, 283
- Kalomeni, B., Nelson, L., Rappaport, S., et al. 2016, *ApJ*, 833, 83
- Knigge, C. 2006, *MNRAS*, 373, 484
- Knigge, C., Baraffe, I., & Patterson, J. 2011, *ApJS*, 194, 28
- Lipunov, V., Kornilov, V., Gorbovskoy, E., et al. 2010, *Advances in Astronomy*, 2010, 349171
- Marcy, G. W., Lindsay, V., & Wilson, K. 1987, *PASP*, 99, 490
- Margoni, R., & Stagni, R. 1984, *A&AS*, 56, 87
- Martini, P., Stoll, R., Derwent, M. A., et al. 2011, *PASP*, 123, 187
- Osterbrock, D. E., Fulbright, J. P., Martel, A. R., et al. 1996, *PASP*, 108, 277
- Pala, A. F., Gänsicke, B. T., Breedt, E., et al. 2020, *MNRAS*, 494, 3799
- Patterson, J. 1979, *ApJ*, 234, 978
- Reinsch, K., & Beuermann, K. 1994, *A&A*, 282, 493
- Robinson, E. L., Shafter, A. W., & Balachandran, S. 1991, *ApJ*, 374, 298
- Rodríguez-Gil, P., Schmidtobreick, L., & Gänsicke, B. T. 2007, *MNRAS*, 374, 1359
- Rodríguez-Gil, P., Shahbaz, T., Torres, M. A. P., et al. 2020, *MNRAS*, 494, 425
- Schneider, D. P., & Young, P. 1980, *ApJ*, 238, 946
- Schwope, A. D. 2018, *A&A*, 619, A62
- Schwope, A. D., Scipione, V., Traulsen, I., et al. 2014, *A&A*, 561, A121
- Shafter, A. W. 1983, *ApJ*, 267, 222
- Shappee, B. J., Prieto, J. L., Grupe, D., et al. 2014, *ApJ*, 788, 48
- Skiff, B. A. 1997, *Information Bulletin on Variable Stars*, 4431, 1
- Szkody, P., Mukadam, A., Gänsicke, B. T., et al. 2010, *ApJ*, 716, 1531
- Szkody, P., Anderson, S. F., Brooks, K., et al. 2011, *AJ*, 142, 181
- Thorstensen, J. R., Charles, P. A., Margon, B., & Bowyer, S. 1978, *ApJ*, 223, 260
- Thorstensen, J. R., Ringwald, F. A., Wade, R. A., Schmidt, G. D., & Norsworthy, J. E. 1991, *AJ*, 102, 272
- Thorstensen, J. R., Schwarz, R., Schwöpe, A. D., et al. 2009, *PASP*, 121, 465
- Tonry, J. L., Denneau, L., Heinze, A. N., et al. 2018, *PASP*, 130, 064505
- Voges, W., Aschenbach, B., Boller, T., et al. 1999, *A&A*, 349, 389
- Warner, B. 1995, *Cambridge Astrophysics Series*, 28
- Watson, C. A., Dhillon, V. S., & Shahbaz, T. 2006, *MNRAS*, 368, 637
- Welsh, W. F., Horne, K., & Gomer, R. 1998, *MNRAS*, 298, 285
- Williams, G. 1983, *ApJS*, 53, 523
- Witham, A. R., Knigge, C., Drew, J. E., et al. 2008, *MNRAS*, 384, 1277
- Wynn, G. A., King, A. R., & Horne, K. 1997, *MNRAS*, 286, 436